Modelling the mobility and dynamics of a large Tahitian landslide using runout distance

Julien Gargani

Modelling the mobility and dynamics of a large Tahitian landslide using runout distance

Julien Gargani[1,2]

[1]Univ. Paris-Saclay, CNRS, Geops, Orsay, France

[2]Univ. Paris-Saclay, Centre d'Alembert, Orsay, France

julien.gargani@universite-paris-saclay.fr

Highlights

- One or a few landslide events created the large scar and mass deposits in Tahiti.
- Peak slide velocity reached 125–250 m/s.
- The high mobility related to an effective basal friction of 0.2–0.3 under submarine conditions.

Abstract

Runout distance was used here to determine whether the large landslide deposit formed several thousand years ago in northern Tahiti was caused by a single or multiple events. Using modelling to quantify the dynamics of this event suggested that a single event or a small number of events (n<10) were responsible, and that the maximum slide velocity was high (>125 m/s) under partially submarine conditions. Such submarine propagation favoured a slower dynamic but a longer runout. The effective basal friction under submarine conditions ranged from $0.2 < \mu < 0.3$.

Keywords : runout, volcano, modelling, landslide, Tahiti

1. Introduction

Various hypotheses have been proposed to explain the triggering of large landslides: (i) ground acceleration due to earthquakes (Keefer, 1994; Roberts and Evans, 2013) or volcanic eruptions (Carracedo et al., 1999), (ii) new stress triggered by dyke intrusion or magma reservoir deformation (Carracedo et al., 1999; Gargani et al., 2006; Hampel and Hetzel , 2008; Le Corvec and Walter, 2009), (iii) increased pore pressure associated with higher rainfall, sea level or lake level (Muller-Salzburg, 1987; Mc Mutry et al., 2001; Cervelli et al., 2002; Kilburn and Petley, 2003; Veveakis et al., 2007; Quidelleur et al., 2008; Crozier, 2010; Gargani et al., 2014; Iverson et al., 2015), and (iv) slope change due to deep erosion or vertical movement. The complexity and inter-relatedness of the processes involved often prevent clear conclusions regarding the precise causes of slope failures.

The nature of large landslide dynamics along the slide path is still under debate because the mobility of these landslides is often larger than expected (Legros, 2002; Lucas and Mangeney, 2007; Iverson et al., 2015). In this study, the mobility of a landslide that occurred in Tahiti, French Polynesia has been investigated. It may be necessary to consider complex processes of various origins to explain such long-distance sliding, such as high basal pressure (Goren and Aharonov, 2007), high-fluidity layer or air-layer lubrification (Johnson, 1978), ground vibration or hydroplaning (Hürlimann et al., 2000), presence of ice or evaporites (Bigot-Cornier and Montgomery, 2007; Crosta et al., 2018), and submarine or aerial propagation (De Blasio, 2011b). The complexity of these processes also leads to difficulties in modelling landslides. For example, the friction angle of actual materials is often higher than that of materials used in simulations. A modelling approach will be conducted to discuss and discriminate the triggering of the landslide.

Several studies have proposed that deposit geometry could provide indications of landslide dynamics (Puga-Bernabéu et al., 2017; Crosta et al., 2018; Collins and Reid, 2020). For example, runout distance may relate to landslide dynamics and can be used to determine the processes involved (Crosta et al., 2018) as it may depend on the effective friction during sliding (Staron and

Lajeunesse, 2009). In this study, the runout distance will be used to discuss the dynamic of the Tahiti landslide. The spreading of landslide material may reflect the processes involved (Puga-Bernabéu et al., 2017; Collins and Reid, 2020). Although morphologic features represent a good set of observable data for past landslides, in the case of large landslides, it may be difficult to discriminate between the specific mobility of the material and the normal spreading of a large volume of material when using morphological data. In addition, large landslide dynamics are difficult to understand due to a lack of accurate data, as deformation and erosion may have affected their morphological characteristics following landslide occurrence (Menendez et al., 2008). Moreover, the rarity of these events reduces the chances of direct observation and thus hinders understanding; dedicated studies are primarily based on past events (Puga-Bernabéu et al., 2017). Large landslides have been observed and studied since several decades, first in aerial cases, for example for the Saidmarreh landslide in Iran (Harrison and Falcon, 1937 ; Roberts and Evans, 2013) or the Blackhawk landslide in California (Shreve, 1968; Johnson, 1978), then under submarine conditions. Large landslide morphology is often recorded only in part due to the difficulty of access, as most cases are located underwater (Abril and Periáñez, 2017), are covered by more recent sediments or lava flows, or are located on other planets like Mars (Quantin et al., 2004). In the present case, the landslide deposits are located under water and the scar is now full of lava. Furthermore, landslide scar and mass transport deposit could represent the consequences of several events triggering the development of complex morphologies (Johnson and Campbell, 2017). Given these observational difficulties, it is not always easy to discriminate morphologies generated by a single landslide from those generated by multiple events. Based on a modelling approach, the study aim is to discriminate between scenarios that advocate for a single events from those that propose that multiple events take place in the case of the Tahiti landslide deposits.

Field studies, geochronological results, and bathymetric data suggest that a large mass displacement took place in Tahiti 872 ± 10 kyr ago (Clouard et al., 2001; Hildenbrand et al, 2004,

2006). However, the cause of the original slope destabilisation and the resulting landslide dynamics have never been precisely constrained. First, it is not clear whether this landslide scar and associated deposits are the consequence of a single large event, a few moderate events, or many small events. Second, the velocity of the Tahitian slide has never been quantified. Field investigations and seismic observations have constrained the geometry of past landslides but have not focused on quantitatively describing their dynamics, while modelling allows the quantitative assessment of slide velocity along the path. Landslide speed has often been estimated for smaller landslides (Rodriguez et al., 2017; Salmanidou et al., 2018), but data and simulations are less common for large landslides. Third, the influence of submarine versus aerial propagation on the velocity of large landslides is unclear, as the former results in increased drag force and decreased frictional force due to the incorporation of water into the slide; interactions between these factors can generate diverse dynamics.

Numerical experiments could provide a complementary approach to previous analyses of the Tahitian landslide scar and related deposits, potentially allowing the validation of a specific scenario and providing quantitative insights. Therefore, this study aimed to (i) discriminate between three hypotheses for this landslide's dynamics (single large event, few moderate events, or many small events) and (ii) estimate the maximum slide velocity.

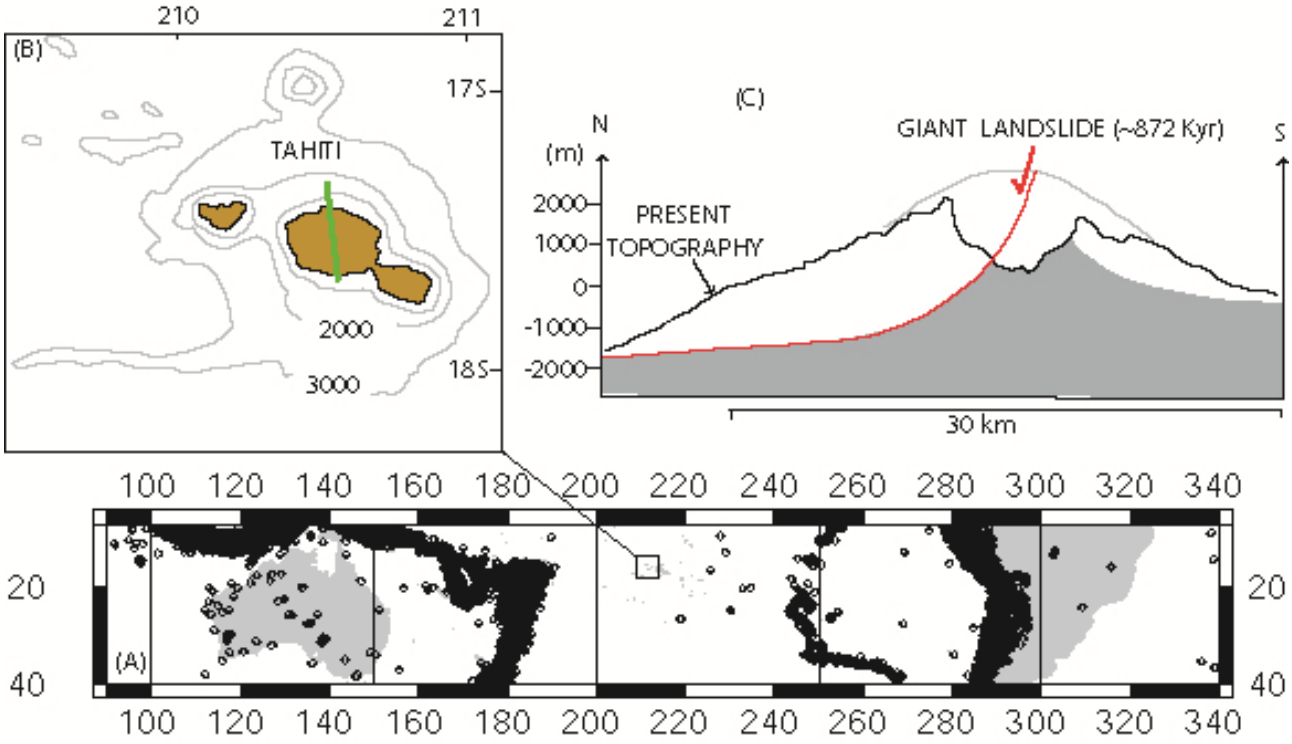

98

99 *Fig. 1: General context for the large Tahitian landslide. (A) Location of Tahiti (17.70° N,*
100 *149.40° E), circles represent the seismicity from 1997 to 2007 with a magnitude M>4*
101 *(seismological data from the USGS Earthquake Database). (B) Tahiti-Nui Island and location of*
102 *cross-section, (C) Schematic cross-section of the giant landslide.*

103

104 **2. Geomorphic patterns and geological structure**

105 The study area is located in the southern Pacific Ocean (Fig. 1A). Several submarine
106 landslides occurred in French Polynesia (Clouard and Bonneville, 2004), whose archipelago
107 includes the volcanic island of Tahiti. Regionally, the Society volcanic chain consists of numerous
108 volcanic islands and seamounts are aligned from northwest to southeast, with ages increasing to the
109 northwest (Patriat et al., 2002). Tahiti is composed of two coalescent volcanoes, Tahiti-Nui to the
110 northwest and Tahiti-Iti to the southeast (Clouard et al., 2001) with steep slopes. These two
111 volcanoes are connected by an isthmus. Tahiti-Nui (Fig. 1B) constitutes the youngest extinct
112 volcano of the Society volcanic chain and is located near the Society hotspot (Duncan and
113 McDougall, 1976).

Lateral collapses are visible on the northern and southern slopes of the main shield volcano (Clouard et al., 2001). The southern collapse occurred between 650 and 850 kyr (Clouard et al., 2001), while the northern collapse occurred around 0.872 ± 0.01 Ma ago (Hildenbrand et al., 2004). These landslides are debris avalanche along listric faults (Clouard and Bonneville ; Hildenbrand et al., 2008). The southern landslide deposits extend up to 60 km away from the island's shore (Clouard and Bonneville, 2004). The maximum runout distance of the northern landslide front reached ~70–80 km, while the runout distance of the centre of mass was ~40 km (Fig. 2). The northern landslide involved volcanic rock several hundreds of metres thick, with a maximum deposit width of ~80–90 km. The volume of the scars are smaller than the volume of the deposits, respectively ~300-460 km^3 and 800-1150 km^3 (Clouard et al., 2001 ; Clouard and Bonneville, 2004 ; Hildenbrand et al., 2008). The Tahitian landslides may have been triggered by a paleoclimatic change (Quidelleur et al., 2008) or by the repeated intrusions of magma inside the main rift zone (Clouard and Bonneville, 2004).

Following the landslide, a second shield developed in the northern depression and dykes were generated on the depression's rims (Hildenbrand et al., 2004). Lava and breccias flowed into these depressions, filling them progressively (Hildenbrand et al., 2008). The present slope of the volcanic edifice ranges from 8–12°, similar to conditions before the large collapse (Hildenbrand et al., 2004 and 2006). The slope is steeper than in Hawaii, probably due to the viscosity of the lava, which is higher for those in Tahiti (Craig, 2003). Rocks from the volcanic system are basalts transitional to tholeiites, alkali basalts, basanites, picrites and evolved lavas (Duncan et al., 1994).

Erosion process are still active on the island. The initial formation of valleys take place rapidly and erosion is faster here than in Hawaii (Craig, 2003). In Tahiti, the recession of the fluvial knickpoints was initiated by a sea level drop of around 135 m, 20 ky ago (Ye et al., 2013). Littoral cliffs have been shaped by marine erosion 7kyr ago (Ye et al., 2013). Climatic conditions are characterized by heavy rainfall (ORSTOM, 1993). The rainwater percolates down through the substrate (Menard, 1986) covered in lava and scoria. Groundwater seeps downward in the upper

slopes via shallow hollows, macropores and flow paths (Craig, 2003). Saturated subsurface flow cause an erosional break in the soil where a channel will begin (Craig, 2003).

This volcano is located in an area where no significant seismicity has been recorded due to its intraplate location (Fig. 1A) and where tectonic deformation is negligible. Subsidence has been measured as 0.25 mm/yr (Bard et al., 1996) and 0.37 mm/yr (Fadil et al., 2009; Thomas et al., 2012). These conditions favour reef formation. There have been no dyke intrusions or volcanic eruptions recorded during the past thousands years, nor any uplift of the volcanic edifice due to magma reservoir activity.

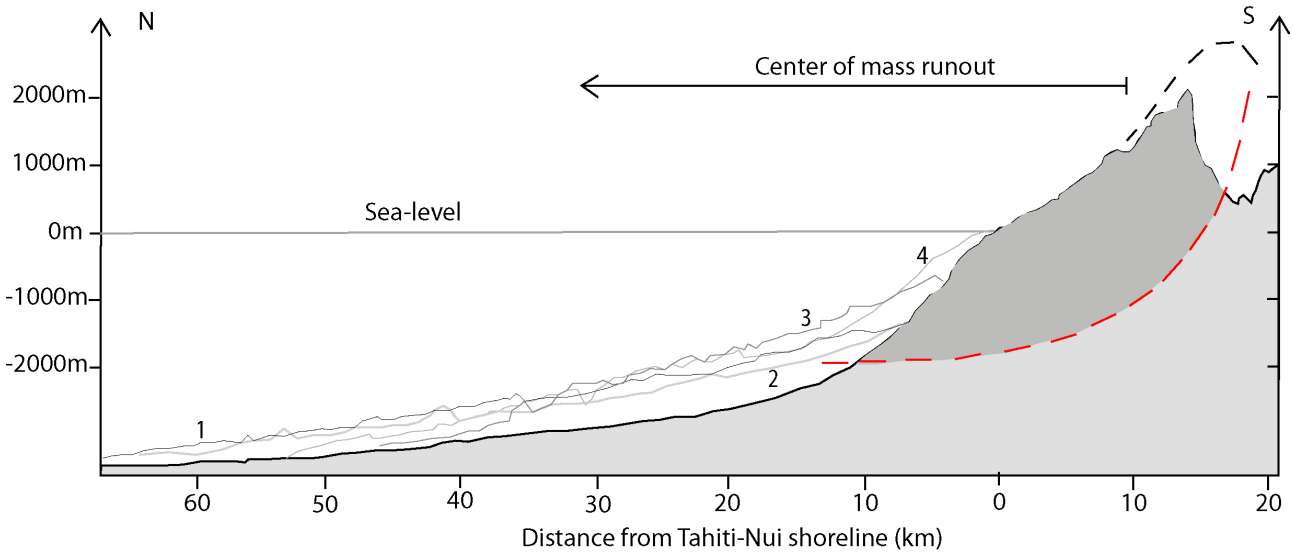

Fig. 2: Longitudinal profiles along the large Tahitian landslide, from which the runout of the centre of mass was estimated as 40 ± 5 km (modified from Hildenbrand et al., 2008).

3. Modelling approach

The mobility of the landslide was modelled in order to study various processes explaining the significant runout distance *L* and to assess the different event scenarios. The model analysed the propagation conditions for three cases: (i) completely subaerial, (ii) completely subaqueous, and (iii) subaerial initiation and subsequent subaqueous propagation.

159 The role of landslide volume on mobility has been investigated by several studies (Goren
160 and Aharonov, 2007; Brunetti et al., 2009; De Blasio, 2011b), which showed that runout is
161 proportional to material volume and that there is an apparent decrease of basal friction (μ~H/L,
162 where H is the height) in relation to increased rock volume. Nevertheless, even if complex thermo-
163 poro-elastic mechanisms (lubrication by high pressure at the base, the presence of evaporites or ice,
164 local melting, ground vibration, trapped air, etc.) are used to explain this phenomena, other studies
165 have shown that slope path geometry and unconsolidated mass spreading play a significant role in
166 describing mobility (Staron and Lajeunesse, 2009). In other words, mobility is controlled primarily
167 by sliding processes in relation to classical friction laws and spreading processes in the case of large
168 volume landslide as in other cases (Staron and Lajeunesse, 2009; Salmanidou et al., 2018).
169 Subaerial sliding along a slope θ was modelled using the weight W of the sliding block and
170 the frictional force R at the base of the sliding block. To simulate the effects of a subaqueous
171 environment, hydrostatic uplift due to buoyancy and the drag force F_D due to seawater were also
172 incorporated (Fig. 3). The latter was based on a classical fluid mechanics approach (Hürlimann et
173 al., 2000):

174 $$F_D = 0.5K \rho_f v^2 A \qquad (1)$$

175 where K is a dimensionless shape coefficient for drag and skin friction, ρ_f is the density of the fluid
176 (i.e. water density if subaqueous or air density if subaerial), v is the sliding block velocity and A is
177 the surface of the sliding block in contact with the fluid opposing the movement. The value of K
178 ranges from 0–2 (Hürlimann et al., 2000).
179 The equation of motion (Hürlimann et al., 2000) was defined as:

180 $$\frac{dv}{dt} = [g(\rho - \rho_f)(\sin\theta - \mu\cos\theta) / \rho] \quad - [\, 0.5\,(K / l)\,(\rho_f / \rho)\, v^2\,] \qquad (2)$$

181 where t is time, g is gravity, θ is the slope, μ is the coefficient of friction, l is the length of the body,
182 and ρ is the density of the sliding block.
183

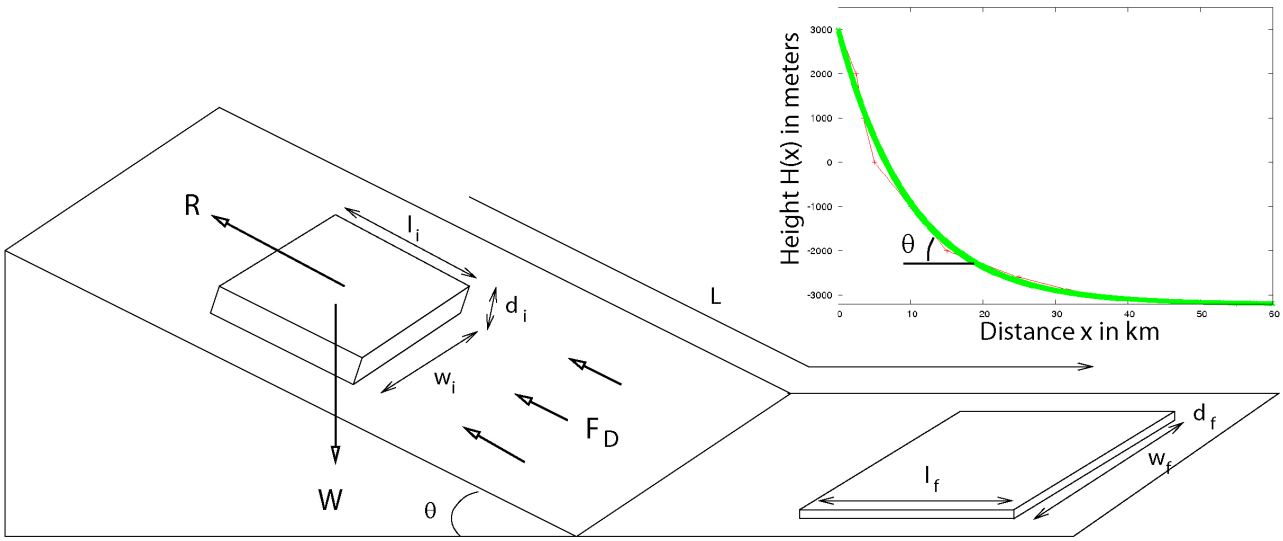

Fig. 3: Geometrical parameters and forces applied to the landslide model along with the simulated path geometry, based on the equation $H(x) = H_0 \exp(x/l_0)$, where $H_0 = 6.2$ km and $l_0 = 10$ km.

In the model, the transition from subaerial to subaqueous sliding was immediate without loss of energy. For simplicity, the slope path was represented by an exponential function, $H(x) = H_0\exp(x/l_0)$, where $H(x)$ is the height of the terrain and x is distance along the path (Fig. 3), H_0 is the initial height, and l_0 is a length that allows to the curvature to fit the slide path (De Blasio, 2011a). These geometric parameters were set as $H_0 = 6.2$ km and $l_0 = 10$ km and allow to fit the real slope (Fig. 3). The density of the sliding block (composed of volcanic rocks) was considered constant at 2800 kg/m^3 (Hürlimann et al., 2000). The density of the fluid ρ_f was set as 1000 kg/m^3 for subaqueous sliding and 0 kg/m^3 for subaerial sliding (Hürlimann et al., 2000). The geometry of the sliding body was characterised by an initial geometry (initial width w_i, initial length l_i, and initial thickness d_i), a final geometry (final width w_f, final length l_f, and final thickness d_f), and a sliding length L (also referred to as runout) (Fig. 3). These parameters were estimated from geomorphologic and bathymetric data (Hildenbrand et al., 2004, 2006). The runout considered here

was that of the centre of mass, not the maximum runout of the slide front.

The large landslide's initial conditions were estimated as width w_i = 25 km, length l_i = 20 km, and thickness d_i = 2000 m, the final geometry was estimated as w_f = 90 km, l_f = 70 km, and d_f = 160 m, and the sliding distance of the centre of mass was estimated as $L = 40 \pm 5$ km. The volume of the sliding block was identical at the initial and final states. The temporal evolution of the geometrical parameters from the initial state to the final state was assumed to be linear. Due to the short duration of the events considered (300 s < t < 850 s), as defined by the simulations, this assumption did not significantly influence the maximum velocity and runout distance. Even if the real value was uncertain, the influence of the geometrical parameters was less significant (in the range of values tested) with respect to the mobility than the friction μ and the hydrodynamic factor K.

The parameters selected for the mobility analysis were the ratio between the hydrodynamic coefficient and the length of the sliding block (K/l) and the friction μ. The first parameter is known to strongly influence sliding dynamics under subaqueous conditions (Hürlimann et al., 2000; De Blasio, 2011a). Assuming a parallelipedic shape of length l, width w, and thickness d, $K/l = C_D/l + C_S/d + 2C_S/w$, where C_D is the drag coefficient and C_S is the skin coefficient. The drag coefficient can be calculated using $C_D = 1.95 - 0.77d/w$ (De Blasio, 2011a). The skin coefficient ranges from $0.002 < C_S < 0.006$ (De Blasio, 2011a). Under these assumptions, the parameter K/l ranges from 5.10^{-5} m^{-1} to 5.10^{-4} m^{-1}, similar to those used by Hürlimann et al. (2000) ($K/l = 2.10^{-4}$ m^{-1} and $K/l = 2.10^{-3}$ m^{-1}). Under subaerial conditions, the coefficient $K/l = 0$ m^{-1}.

The value of friction μ can range from 0.6–0.85 (Bayerlee's law) for dry subaerial conditions of intact rocks and has been estimated as low as 0.0025–0.08 for subaqueous conditions in specific cases (Hürlimann et al., 2000; De Blasio, 2011a) such as hydroplaning or the presence of evaporites. In this study, the basal friction μ was set at an intermediate value of 0.2–0.3 under subaqueous conditions instead of 0.6 under subaerial conditions. The former value corresponded to an angle of friction of ϕ = 11–17° in accordance with the value considered appropriate for highly

weathered and fragmented volcanic rock (Rodriguez-Losada et al., 2009).

Alternatively, a viscous rheology could be considered to simulate the complex behaviour of the landslide using the Bingham law, in which the shear stress:

$\tau = \eta\, dv/dz + \tau_0$, if $\tau > \tau_0$

and $\tau = 0$, if $\tau < \tau_0$,

where η is the viscosity, τ_0 is the yield stress, v is the velocity of the landslide, and z is the vertical distance. For a thickness h and a depth-averaged velocity v, the shear rate can be estimated by $dv/dz \approx 2v/h$ (Pelletier et al., 2008). The resulting shear stress thus becomes $\tau = 2\eta\, v/h + \tau_0$. Therefore, an increase in viscosity will increase the difficulty of landslide propagation, as expected. Under this assumption, landslide dynamics can be modelled by:

$$\frac{dv}{dt} = [g(\rho - \rho_f) \sin\theta / \rho] - [\, 2\eta v / (\rho h^2) + \tau_0 / (\rho h)\,] - [\, 0.5\, (K / l)\, (\rho_f / \rho)\, v^2\,] \quad (3)$$

where the first term on the right side is due to the weight, the second term is due to the viscous behaviour of the landslide, and the third term is due to water drag.

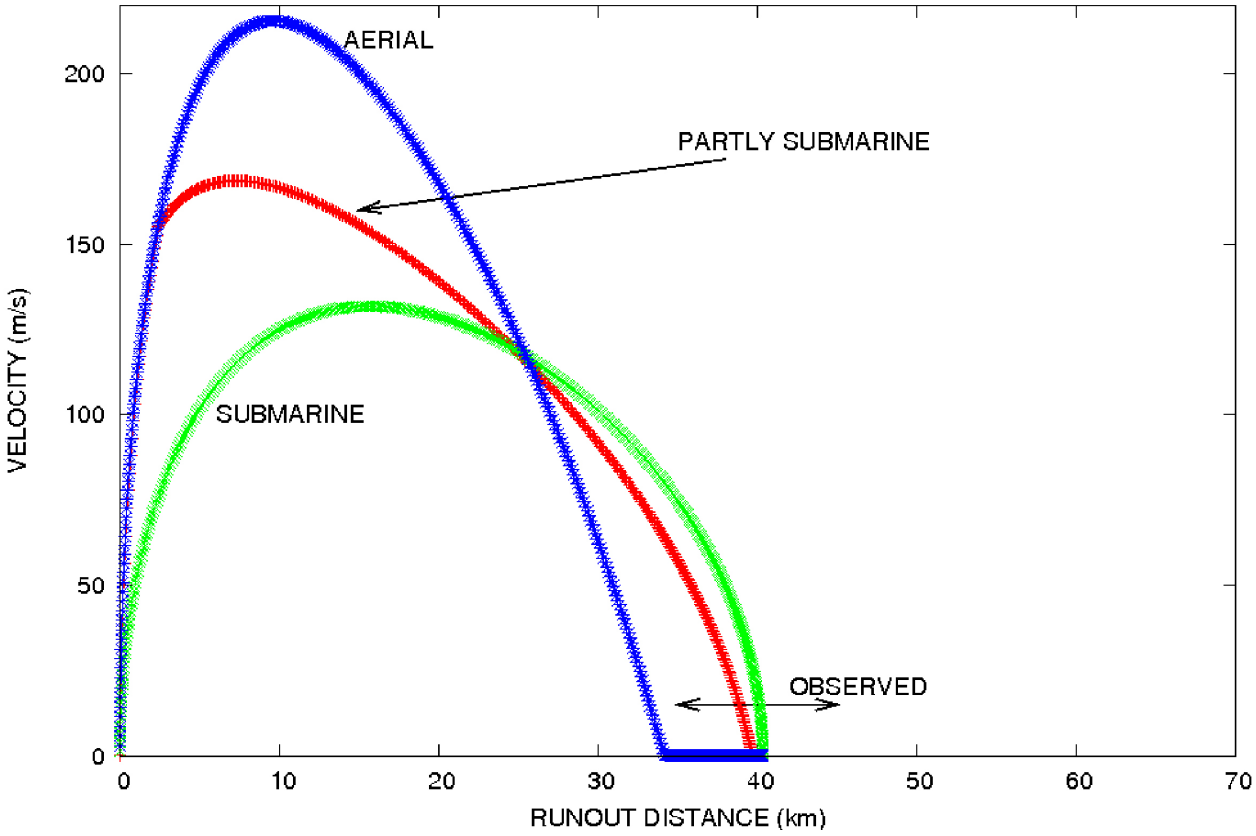

Fig. 4: Influence of three simulated propagation conditions: aerial, submarine, and partly submarine (5 km aerial, then submarine). $K/l = C_D/l+C_S/d+2C_S/w$ for all cases. $\mu = 0.27$ ($\phi = 15.5°$) under submarine conditions and $\mu = 0.6$ under aerial conditions. $w_i = 25$ km, $l_i = 20$ km, and $d_i = 2$ km. Observed runout of the landslide's centre of mass is assumed to be 40 ± 5 km.

4. Results

The landslide propagated mostly under subaqueous conditions although the slide may have initiated under subaerial conditions. This study's model assumed that the slide material entered into the sea after 5 km and compared the effects of subaqueous and subaerial propagation. The landslide's submarine and partly submarine mobility was of the same order of magnitude (Fig. 4). The runout distance and slide time could be higher under subaqueous conditions than under subaerial conditions, assuming a reduction of basal friction under submarine conditions from 0.6 to 0.3 (Fig. 4). The subaerial propagation of the landslide showed a higher maximum velocity than

submarine propagation, despite the reduction of effective basal friction simulated in the latter (Fig. 4). When the effect of hydroplaning was not considered (μ was constant), aerial propagation was longer than submarine propagation due to the increased hydrodynamic drag force. The maximum aerial velocity was ~215 m/s, but only 170 m/s for a partly submarine landslide and 125 m/s for a submarine landslide (Fig. 4). Entering the water generally resulted in decreased velocity (Fig. 5). However, if the volume of material was significant (L = 20 km, V = 1000 km^3), the velocity of the landslide was able to continue increasing after entering the water (although at a smaller rate) for ~3 km due to the inertia of the sliding material (Fig. 6). The slide time was higher under subaqueous conditions than under subaerial conditions (Fig. 5).

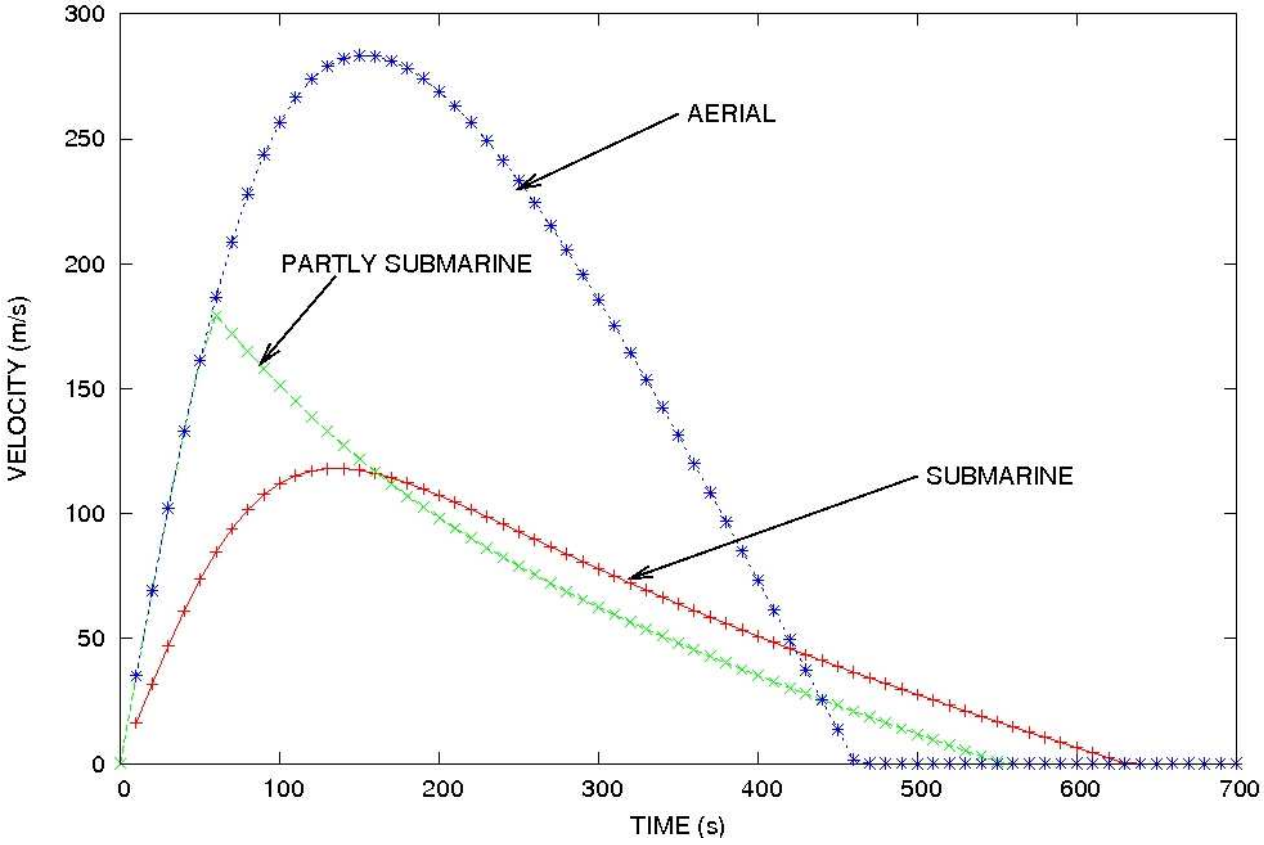

Fig. 5: Landslide velocity over time under three different propagation conditions: aerial, submarine, and partly submarine (5 km aerial, then submarine). The drag friction was set equal to K/l = 0.0004. μ = 0.2 (ϕ = 11.3°) under submarine conditions and μ = 0.6 under aerial conditions.

271 w_i = 25 km, l_i = 20 km, and d_i= 2 km.

272 A landslide with a large initial volume V of 1000 km^3 (volume $V = w$ x l x d = 25 km x 20
273 km x 2 km) allowed the runout distance of ~40 km observed offshore of Tahiti with a basal friction
274 μ = 0.27 (Fig. 6A), but not with a basal friction μ = 0.2 (Fig 6B). Smaller landslides with a length
275 l/10 or l/100 had a runout L smaller than a bigger landslide with an initial length l under partly
276 submarine conditions. For a repetition of n = 10 small landslides with a length l/10, a width w, and a
277 thickness d (w x l/10 x d = V/10), the total deposit volume (V_{total} = 10 x V/10) was equivalent to a
278 unique landslide with a volume V. Ten landslides with a volume V/10 had an expected runout of
279 ~25 km when the basal friction μ = 0.27, below the observed runout distance observed (Fig. 6A).
280 However, when the basal friction μ = 0.2, the runout distance of landslides with volume V/10 fit the
281 observed runout data (Fig. 6B). For a volume of each landslide of V/100 (i.e. the length of each
282 landslide became ~l/100, but the initial width w as well as the thickness d was the same as for
283 landslides with volumes V and V/10), the calculated runout distance was ~20 km for μ = 0.27 and
284 30 km for μ = 0.20, below the observed runout distance (Fig 6). For l/100, only a very small basal
285 friction $\mu << 0.2$ was able to fit the observed runout of the centre of mass. The number of landslides
286 with a volume V/100 necessary to obtain the observed volume of deposits was 100. In all
287 simulations, the maximum velocity of the landslides ranged from 180–200 m/s.

288 In the Tahitian case considered here, the final deposit's centre of mass was located ~40 km
289 from its initial position and the front of the slide propagated ~80 km. An effective basal friction μ of
290 0.2–0.3 under submarine conditions allowed the simulation to fit the observed runout distance.
291 Reduced basal friction permitted the simulation of hydroplaning effects. Conversely, increasing
292 aerial propagation increased the maximum velocity of the slide but slightly reduced the runout
293 distance of the centre of mass.

294

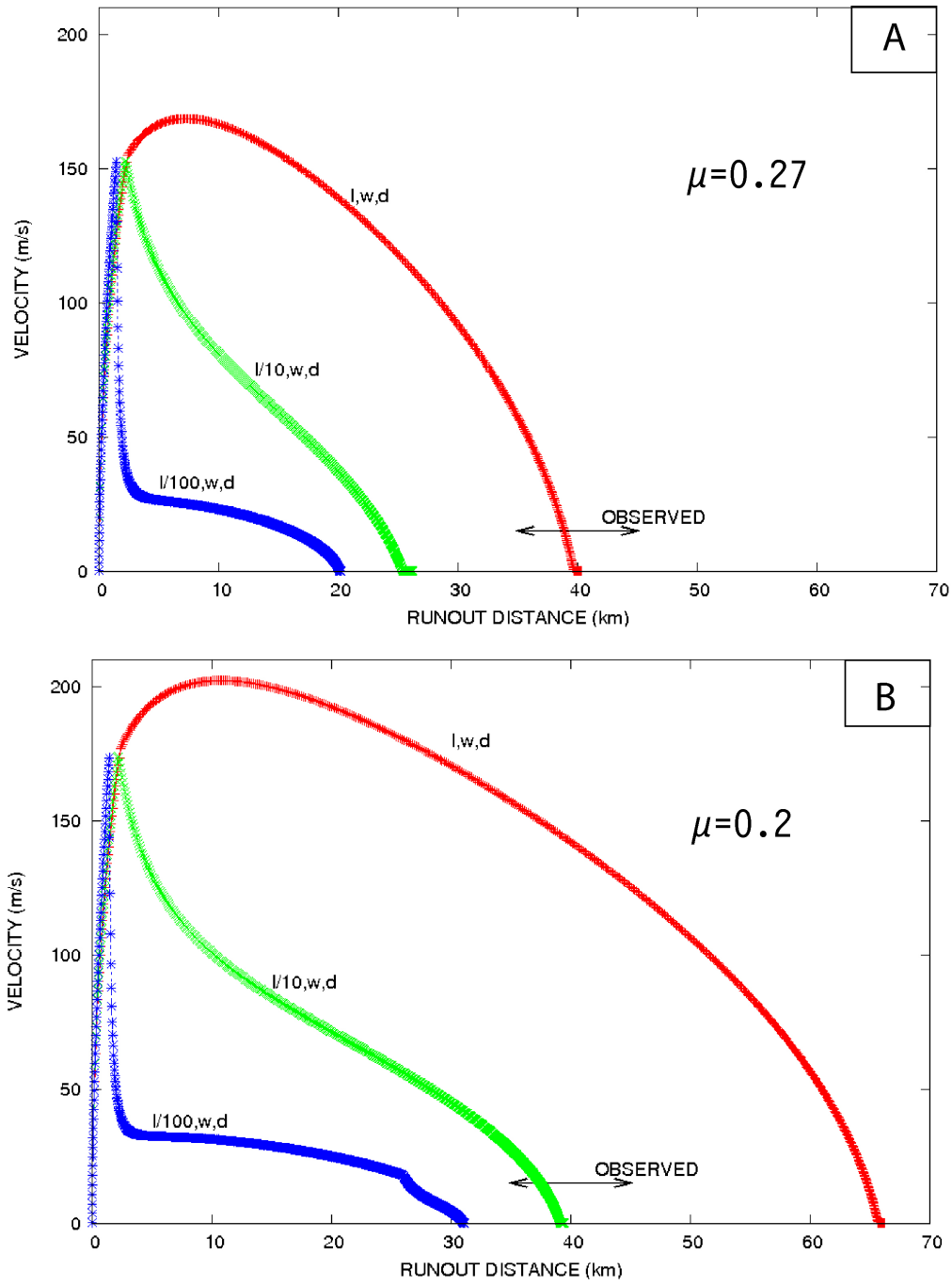

Fig. 6: Effect of landslide volume on landslide dynamics for three volumes and two friction values: (A) μ =0.27 (ϕ =15.5°) under submarine conditions and (B) μ =0.2 (ϕ =11.3°) under submarine conditions. In both cases, propagation initiated under aerial condition but transitioned to submarine conditions after 5 km. The water effective drag coefficient was defined as $K/l=C_D/l+C_S/d+2C_S/w$. *where* w_i = 25 km, d_i= 2 km, *and* l_i = 20 km, 2 km, *or* 0.2 km. *The observed runout of the landslide centre of mass was* 40 ± 5 *km. Under aerial conditions, the basal friction* μ =0.6.

The mechanical behaviour of the highly fragmented sliding material was accurately simulated by low effective friction and allowed explanation of its significant mobility. Alternative modelling experiments including more complex rock behaviour may also explain the dynamics of this landslide (Fig. 7). For example, viscous behaviour could also explain the observed runout of the centre of mass (Fig. 7). There is an abrupt decrease of the velocity from the aerial part to the submarine part. In this case, the submarine velocity was < 50 m/s for almost all slide paths (Fig. 7) and smaller than for non-viscous conditions; this is near the peak velocity obtained for other submarine landslides with a smaller size (L'heureux et al., 2013; Rodriguez et al., 2017; Abril and Periañez, 2017; Salmanidoue et al., 2018; Sawyer et al., 2019).

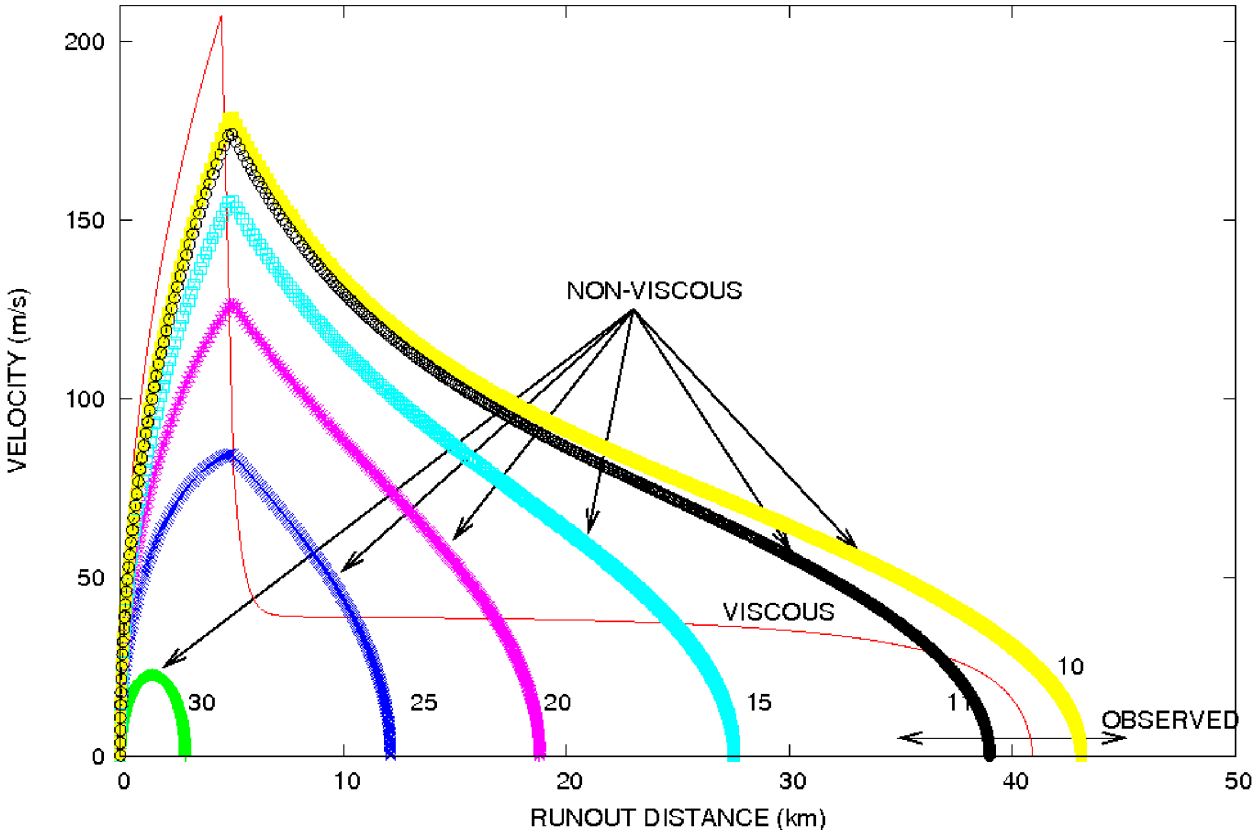

Fig. 7: Modelled landslide velocity vs. runout distance (η =5 MPa.s, τ_0 = 0.5 Mpa) for viscous and various non-viscous rheologies for different angles of internal friction (ϕ = 30°, 25°, 20°, 15°, 11°, and 10°). In all cases, the landslide propagates aerially for the first 5 km, then transitions to submarine conditions. $K/l = C_D/l + C_S/d + 2C_S/w$. w_i = 25 km, l_i = 2 km, d_i= 2 km. The observed runout of the landslide centre of mass is 40 ± 5 km.

5. Discussion

Previous studies have suggested that landslide propagation under submarine conditions could result in longer runout distances and the occurrence of hydroplaning (Locat and Lee, 2002; De Blasio, 2011b; Hürlimann et al 2000). However, in several case where no hydroplaning occurred, submarine propagation reduced the runout distance (Gargani et al., 2014). Other lubrification effects could also explain decreases in basal friction under aerial (Johnson, 1978) or submarine conditions. The spreading of a large volume of material could partially explain the long apparent runout of the landslide's front (Johnson and Campbell, 2017).

This study's modelling showed that slide velocity decreased (Fig. 5) or reduced its acceleration (Fig. 4) after entering the water, as the drag force generated by water is more efficient than that of air; the former could be significant at high velocities. Previous studies suggested that subaerial mass acceleration can be much greater than submarine mass acceleration yet (Kafle et al., 2016). Furthermore, the presence of water could generate a counterintuitive effect by increasing the runout distance (Fig. 4). Such significant runout under subaqueous conditions has been explained by hydroplaning (De Blasio, 2011a). The competition between drag and friction force on one hand, and gravity and buoyancy on the other, could explain the high runout under subaqueous conditions seen in this study. Under such conditions, the propagation along the path was slower but lasted longer (Fig. 5), as shown by previous studies (Hürlimann et al., 2000; De Blasio, 2011b). When the volume and length of a landslide are large, the inertia of the sliding block could allow a reduced effect of the drag force when entering the water, such that the sliding block speed is not reduced abruptly when the propagation becomes submarine (Fig. 6).

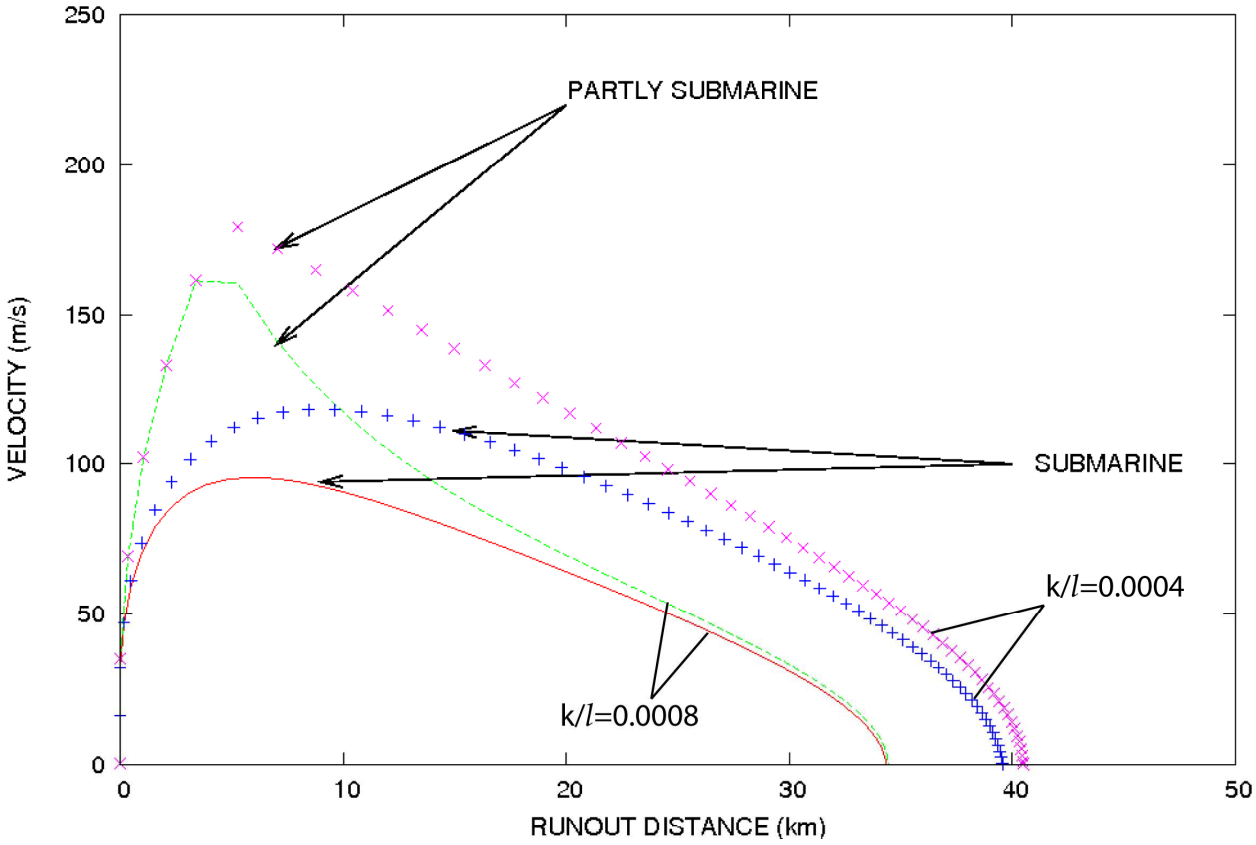

Fig. 8: Influence of the effective drag coefficient k/l on landslide dynamics for submarine and partly submarine propagation. For aerial propagation, the effective drag coefficient k/l=0. μ=0.2 under submarine condition and μ=0.6 under aerial condition.

One of this study's main questions relates to whether the Tahitian landslide deposits considered here were formed through a single slide event or multiple events. If the former, the runout distance of ~40 km could be easily achieved with a friction $\mu = 0.27$ under submarine conditions (Fig. 6A). However, under this condition, other landslide geometries did not fit the observed runout distance. The simulated runout was lower for smaller landslide geometries, as an increasing length l decreases the ratio K/l. The drag coefficient is significantly reduced when the length of the sliding block is increased. Equation (2) shows that larger landslides are capable of propagating longer distances than smaller ones (Fig. 6). If all other parameters are equal, an increase in the effective drag coefficient K/l will decrease propagation distance (Fig. 8). A decrease

355 in *K*/*l* by a factor of two can increase the runout of the centre of mass by a factor of ~1.2. In this
356 model, the width of the landslide had only a small influence on the runout because the skin
357 coefficient C_S was small in comparison with the drag coefficient C_D.

358 Nevertheless, it may be possible that the deposits were formed by a limited number of
359 landslide events (n<10). Indeed, the observed runout distance can also be explained by the
360 occurrence of ten separate landslides with a length of ~2 km using a basal friction $\mu = 0.2$ under
361 submarine conditions (Fig. 6B). However, this multi-slide scenario (n > 10) is less realistic, because
362 it implies that the basal friction became very low ($\mu << 0.2$, $\phi < 10°$) in order to fit the observed
363 runout. Although the occurrence of a single event was difficult to prove, the modelling showed that
364 a reduced number of events (<10) was necessary to reproduce the observed runout distance.
365 Therefore, these results support the proposal that a single event or a reduced number of events
366 generated the large debris apron morphology. The ability of few events to form moderate to large
367 landslide morphology (i.e. scars and mass transport deposits) has been advocated in several specific
368 cases using more accurate geomorphological data and observations (Cauchon-Voyer et al., 2011 ;
369 Puga-Bernabéu et al., 2017 ; Collins and Reid, 2020). For example, some studies of the Oso
370 landslide have advocated for two larges, distinct failure events separated by a few minutes, whereas
371 others studies suggested that the vast majority of landslide activity occurred within the initial
372 minute (Collins and Reid, 2020). In comparison, the Gloria Knolls landslide consisted of three
373 events (Puga-Bernabéu et al., 2017).

374 Extremely small basal friction values are not necessary to explain the large runout of the
375 Tahitian landslide's centre of mass, which primarily propagated under submarine conditions.
376 Values of $0.2 < \mu < 0.3$ corresponded to an angle of internal friction from 11–17°, as expected for
377 very weathered basalt or pyroclastic rocks (Rodriguez-Losada et al., 2009). To reach these values,
378 the landslide may have caused significant fragmentation of the material. The numerous fractures
379 and long polygenic history of the volcanic edifice probably contributed to the presence of weak
380 material (Hildenbrand et al. 2004). The humid climate of Tahiti could also explain the highly

weathered and altered nature of the rocks, which contributed to the presence of weak material from a mechanical perspective.

The estimated slide peak velocity ranged from 125–250 m/s, within the range of other large landslide peak velocities observed or calculated in volcanic contexts (Voight et al., 1983; Hürlimann et al., 2000) but higher than that of smaller submarine landslides (20–50 m/s) (L'heureux et al., 2013; Rodriguez et al., 2017; Abril and Periañez, 2017; Salmanidoue et al., 2018; Sawyer et al., 2019). The significant mass displacement may have triggered an isostatic rebound (Gargani, 2004, 2010). A tsunami should also have occurred after the landslide as has been estimated for other comparable events (Bohannon and Gardner, 2004; Rodriguez et al., 2017).

6. Conclusion

The velocity of the Tahitian landslide exceeded 125 m/s, allowing the fragmentation of highly weathered rocks. The effective basal friction for submarine propagation was relatively low ($0.2 < \mu < 0.3$), enabling significant mobility for the centre of mass (~40 km^3) and suggesting that hydroplaning occurred under submarine conditions. The long runout length of the centre of mass also suggested that the landslide deposit was the consequence of a single event or a reduced number of events (n<10). The initial length of the landslide varied between $l/10 < l_i < l$, where l = 20 km for a total volume V ~ 1000 km^3. The significant mobility of the material and the slide dynamics constrained the geometry of the mass transport deposit.

Declarations of interest: None

Funding : This research did not receive any specific grant from funding agencies in the public, commercial, or not-for-profit sectors.

Acknowledgements: The editor and two anonymous reviewers are thanked for their help and their

408 constructive comments.

409

410

411 **References**

412

413 Abril JM, Periáñez R., 2017. An Exploratory Modelling Study on Late Pleistocene Mega-Tsunamis
414 Triggered By Giant Submarine Landslides in the Mediterranean. Ann Limnol Oceanogr 2(1): 007-
415 024. DOI: 10.17352/alo.000005

416

417 Bard E., Hamelin B., Arnold M., Montaggioni L., Cabiosh G., Faure G., Rougerie F., 1996.
418 Deglacial sea-level record from Tahiti corals and the timing of global meltwater discharge. Nature
419 382, 241-244.

420

421 Bigot-Cornier F., Montgomery D.R., 2007. Valles Marineris landslides: Evidence for a strength
422 limit to Martian relief? Earth and Planetary Science Letters 260, 179-186.

423

424 Bohannon R.G. and Gardner J.V., 2004. Submarine landslides of San Pedro Escarpment, southwest
425 of long Beach, California. Marine Geology 203, 261-268.

426

427 Brunetti M.T., Guzzetti F., Rossi M., 2009. Probability distributions of landslide volumes. Nonlin.
428 Processes Geophys, 16, 179-188.

429

430 Carracedo J.C. Day S.J., Guillou H., Pérez Torrado F.J., 1999. Giant Quaternary landslides in the
431 evolution of La Palma and El Hierro, Canary Islands. Journal of Volcanology and Geothermal
432 Research 94, 169-190.

433

Cauchon-Voyer G., Locat J., Leroueil S., St-Onge G., Demers D., 2011. Large-scale subaerial and submarine Holocene and recent mass movements in the Betsiamites area, Quebec, Canada. Engineering Geology 121, 28-45. doi.org/10.1016/j.enggeo.2011.04.011

Cervelli P., Segall P., Johnson K., Lisowski M., Miklius A., 2002. Sudden aseismic fault slip on the south flank of Kilauea volcano, Nature 415, 1014-1018.

Clouard V., Bonneville A., Gillot P-Y., 2001. A giant landslide on the southern flank of Tahiti Island, French Polynesia. Geophysical Research Letters 28, 2253-2256.

Clouard V., Bonneville A., 2004. Submarine Landslides in French Polynesia. In: Hekinian R., Cheminée JL., Stoffers P. (eds), Oceanic Hotspots, Springer, Berlin, 209-238. https://doi.org/10.1007/978-3-642-18782-7_7

Collins B.D., M.E. Reid, 2020. Enhanced landslide mobility by basal liquefaction: The 2014 State Route 530 (Oso), Washington, landslide. GSA Bulletin; March/April 2020; v. 132; no. 3/4; p. 451–476; https://doi.org/10.1130/B35146.1

Craig D.A., 2003. Geomorphology, Development of running water habitats and Evolution of black flies on Polynesian Islands. BioScience, v.53, n.11, 1079-1093.

Crosta G.B., F.V. De Blasio, P. Frattini, 2018. Global Scale Analysis of Martian Landslide Mobility and Paleoenvironmental Clues, Journal of Geophysical Research: Planets, Volume 123, Issue 4, https://doi.org/10.1002/2017EA000324.

Crozier, M.J., 2010, Deciphering the effect of climate change on landsliding activity : A review. Geomorphology 124, 260-267.

462 De Blasio F.V., 2011a. Landslides in Valles Marineris (Mars): A possible role of basal lubrication
463 by sub-surface ice. Planetary and Space Science 59, 1384-1392.
464
465 De Blasio F.V., 2011b. The aureole of Olympus Mons (Mars) as the compound deposit of
466 submarine landslides. Earth and Planetary Science Letters 312, 126-139.
467
468 Duncan, R.A., McDougall, I., 1976. Linear volcanism in French Polynesia, J. Volcano. Geotherm.
469 Res. 1, 197-227.
470
471 Duncan R.A., Fisk M.R., White W.M., Nielsen R.L., 1994. . Tahiti : Geochemical evolution of a French
472 Polynesia volcano. Journal of Geophysical Research, V.99, n.B12, p.24,341-24,357.
473
474 Fadil, A , Barriot, J., Sichoix, L., Ortega, P., 2009. GPS Subsidence rate of Tahiti : comparison with
475 coral reef stratigraphy. American Geophysical Union, Fall Meeting, abstract #G33B-0647.
476
477 Gargani J., 2004 Modelling of the erosion in the Rhone valley during the Messinian crisis (France),
478 *Quaternary International, 121, 13-22*.
479
480 Gargani J., Geoffroy L., Gac S., Cravoisier S., 2006. Fault slip and Coulomb stress variations
481 around a pressured magma reservoir: consequences on seismicity and magma intrusion. Terra Nova
482 18, 403-411.
483
484 Gargani J., C. Rigollet, S. Scarselli, 2010. Isostatic response and geomorphological evolution of the
485 Nile valley during the Messinian salinity crisis. *Bull. Soc. Geol. Fr.,* 181, n.1, 19-26.
486
487 Gargani J., F. Bache, G. Jouannic, C. Gorini, 2014. Slope destabilization during the Messinian
488 Salinity Crisis. *Geomorphology, v.213, p.128-138*.

Goren L., Aharonov, E., 2007. Long runout landslides : The role of frictional heating and hydraulic difussivity. Geophys. Research Letters 34, L07301, doi:10.1029/2006GL028895.

Guglielmi Y., Cappa F., 2010. Regional-scale relief evolution and large landslides: Insights from geomechanical analyses in the Tinée Valley (southern French Alps). Geomorphology 117, 121-129.

Hampel A., Hetzel R., 2008. Slip reversals on active normal faults related to the inflation and deflation of magma chambers: Numerical modeling with application to the Yellowstone-Teton region. Geophysical Research Letters 35, L07301, doi: 10.1029/2008GL033226.

Harrison V., Falcon N.L., 1937. The Saidmarreh Landslip, South-West Iran. The Geographical Journal. Vol. 89, No. 1, pp. 42-47.

Hildenbrand A., Gillot P-Y., Le Roy I., 2004. Volcano-tectonic and geochemical evolution of an oceanic intra-plate volcano: Tahiti-Nui (French Polynesia). Earth and Planetary Science Letters 217, 349-365.

Hildenbrand A., Gillot P-Y., Bonneville A., 2006. Offshore evidence for a huge landslide of the northern flank of Tahiti-Nui (French Polynesia). Geochemestry, Geophysics, Geosystems 7, Q03006, doi:10.1029/2005GC001003.

Hildenbrand A., Gillot P-Y, Marlin C., 2008. Geomorphological study of long-term erosion on a tropical volcanic ocean island: Tahiti-Nui (French Polynesia). Geomorphology 93, 460-481.

514 Hürlimann M., Garcia-Piera J.O., Ledesma A., 2000. Causes and mobility of large volcanic
515 landslides : application to Tenerife, Canary Islands. Journal of Volcanology and Geothermal
516 Research 103, 121-134.

517

518 Iverson R.M., D.L. George, K.Allstadt, M.E. Reid, B.D. Collins, J.W. Vallance, S.P. Schilling, J.W.
519 Godt, C.M. Cannon, C.S. Magirl, R.L. Baum, J.A. Coe, W.H. Schulz, J.B. Bower, 2015. Landslide
520 mobility and hazards: implications of the 2014 Oso disaster. Earth and Planetary Science Letters
521 412, 197-208.

522 Johnson B., 1978. Blackhawk Landslide, California, USA. Developments in Geotechnical Engineering,
523 Volume 14, Part A, 1978, Pages 481-504.

524

525 Johnson B.C., C.S. Campbell, 2017. Drop Height and Volume Control the Mobility of Long-
526 Runout Landslides on the Earth and Mars. GeophysicalResearch Letters,44.
527 https://doi.org/10.1002/2017GL076113.

528

529 Kafle J., Pokhrel P., Khattri K.B., Kattel P., Tuladhar B.M., Pudasainia S.P., 2016. Landslide-
530 generated tsunami and particle transport inmountain lakes and reservoirs. Annals of Glaciology
531 57(71) 2016, 232-244, doi: 10.3189/2016AoG71A034.

532

533 Kilburn, C.R.J., Petley, D.N., 2003. Forecasting giant, catastrophic slope collapse: lessons from
534 Vajont, Northern Italy. Geomorphology 54, 21-32.

535

536 Keefer D.K., 1994. The importance of earthquake-induced landslides to long-term slope erosion and
537 slope-failure hazards in seismically active regions. Geomorphology 10, 265-284.

538

539 Le Corvec N., Walter T.R., 2009. Volcano spreading and fault interaction influenced by rift zone
540 intrusions: Insights from analogue experiments analyzed with digital image correlation technique.
541 Journal of Volcanology and Geothermal Research 183, 170-182.

542

543 Legros F., 2002. The mobility of long-runout landslides. Engineering Geology 63, 301-331.

544

545 L'Heureux, J.S., Vanneste, M., Rise, L., Brendryen, J., Fors-berg, C.F., Nadim, F.,
546 Longva, O., Chand, S., Kvalstad, T.J., Haflidason, H., 2013. Stability, mobility and
547 failure mechanism for landslides at the Upper Continental Slope off Vesterâlen,
548 Norway. Marine Geology 346, 192-207. doi: 10.1016/j.margeo.2013.09.009
549

550 Locat J., H.J. Lee, 2002. Submarine landslides: advances and challenges. Canadian Geotechnical
551 Journal 39, 193-212.
552

553 Lucas A., A. Mangennoy, 2007. Geophysical Research Letters, v. 34.

554

555 McMutry G.M., Watts P., Fryer G.J, Smith J.R., Imamura F., 2004. Giant landslides, mega-
556 tsunamis, and paleo-sea level in the Hawaiian Islands, Marine Geology 203, 219-233.

557

558 Menard HW. 1986. Islands. New York: Scientific American Library.

559

560 Menendez, I., Silva, P.G., Martin-Betancor, M., Pérez-Torrado, F.J., Guillou, H., Scaillet, S., 2008.
561 Fluvial dissection, isostatic uplift, and geomorphological evolution of volcanic islands (Gran
562 Canaria, Canary Islands, Spain). Geomorphology 102, 189-203.

563

564 Muller-Salzburg L., 1987. The Vajont catastrophe – a personnal review, Engineering Geology 24,
565 423-444.

566

567 ORSTOM] Office de la Recherche Scientifique et Technique Outre-Mer. 1993. Atlas de la Polynésie
568 Française. Paris: Éditions de l'ORSTOM.

569

570 Patriat M., Klingelhoefer F., Aslanian D., Contrucci I., Gutscher M-A., Talandier J., Avedik F.,
571 Francheteau J., Weigel W., 2002. Deep crustal structure of the Tuamotu plateau and Tahiti (French
572 Polynesia) based on seismic refraction data. Geophysical Research Letters 29,
573 doi:10.1029/2001GL013913.

574

575 Pelletier J.D., Kolb, K.J., McEwen A.S., Kirk R.L., 2008. Recent bright gully deposits on Mars:
576 Wet or dry flow? Geology 36, 211-214.

577

578 Puga-Bernabéu A., Beaman R.J., Webster J.M., Thomas A.L., Jacobsen G., 2017. Gloria Knolls
579 Slide: A prominent submarine landslide complex on the Great Barrier Reef margin of north-eastern
580 Australia. Marine Geology 385, 68-83. https://doi.org/10.1016/j.margeo.2016.12.008

581

582 Quantin C., Allemand P., Mangold N., Delacourt, 2004. Ages of Valles Marineris (Mars) landslides
583 and implications for canyon history. Icarus 172, 555-572.

584

585 Quidelleur X., Hildenbrand A., Samper A., 2008. Causal link between Quaternary paleoclimatic
586 changes and volcanic islands evolution. Geophysical Research Letters 35, L02303,

587 doi:10.1029/2007GL031849.

588 Roberts N., Evans S.G., 2013. The gigantic Seymareh (Saidmarreh) rock avalanche, Zagros Fold-
589 Thrust Belt, Iran. Journal of the Geological Society 170(4), 685-700.
590

591 Rodriguez M., Maleuvre C., Jollivet-Castelot M., d'Acrmont E., Rabaute A., Lafosse M., Ercilla G.,
592 Vasquez J-T., Alonso Belén, Ammar Abdellah, Gorini C., 2017. Tsunamigenic submarine
593 landslides along the Xauen-Tofiño banks in the Alboran Sea (Western Mediterranean Sea).
594 Geophysical Journal International 209, 266-281.

595

596 Rodriguez-Losada J.A., Hernandez-Gutérrez L.E., Olalla C., Perucho A., Serrano A., Eff-Darwich
597 A., 2009. Geomechanical parameters of intact rocks and rock masses from the Canary Islands:
598 Implications on their flank stability. Journal of Volcanology and Geothermal Research 182, 67-75.

599

600 Salmanidou D.M., Georgiopoulou A., Guillas S., Dias F., 2018. Rheological considerations for the
601 modelling of submarine sliding at Rockall Bank, NE Atlantic Ocean. Physics of Fluids 30, 030705
602 (2018); https://doi.org/10.1063/1.5009552.

603

604 Sawyer D.E., Mason R.A., Cook A.E., Portnov A., 2019. Submarine Landslides Induce Massive
605 Waves in Subsea Brine Pools. Scientific Reports 9:128, DOI:10.1038/s41598-018-36781-7.

606

607 Shreve, R.L., 1968. The Blackhawk Landslide. Geol. Soc. Am. Special Papers, special paper 108, 47 pp.

608

609 Staron L., Lajeunesse E., 2009. Understanding how volume affects the mobility of dry debris flows.
610 Geophys. Research Letters 36, L12402, doi:10.1029/2009GL038229.

611

612 Thomas A.L., Fujita K., Iryu Y., Bard E., Cabioch G., Camoin G., Cole J.E., Deschamps P., Durand
613 N., Hamelin B., Heindel K., Henderson G.M., Mason A.J., Matsuda H., Ménabréaz L., Omri A.,
614 Quinn T., Sakai S., Sato T., Sugihara K., Takahashi Y., Thouveny N., Tudhope A.W., Webster J.,
615 Westphal H., Yokoyama Y., 2012. Assessing subsidence rates and paleo water-depths for Tahiti
616 reefs using U-Th chronology of altered corals. Marine Geology 295-298, 86-94.

617

618 Veveakis E., Vardoulakis I., Di Toro G., 2007. Thermoporomechanics of creeping landslides: The
619 1963 Vaiont slide, northern Italy. Journal of Geophysical Research 112, F03026,
620 doi:10.1029/2006JF000702.

621

622 Voight B., Janda R.J., Glicken H., Douglass P.M., 1983. Nature and mechanics of the Mount St
623 Helens rockslide-avalanche of 18 May 1980. Géotechnique 33, 243-273.

624

625 Ye F. Y., Barriot J. P., Carretier S., 2013. Initiation and recession of the fluvial knickpoints of the
626 Island of Tahiti (French Polynesia). Geomorphology 186, p. 162-173.

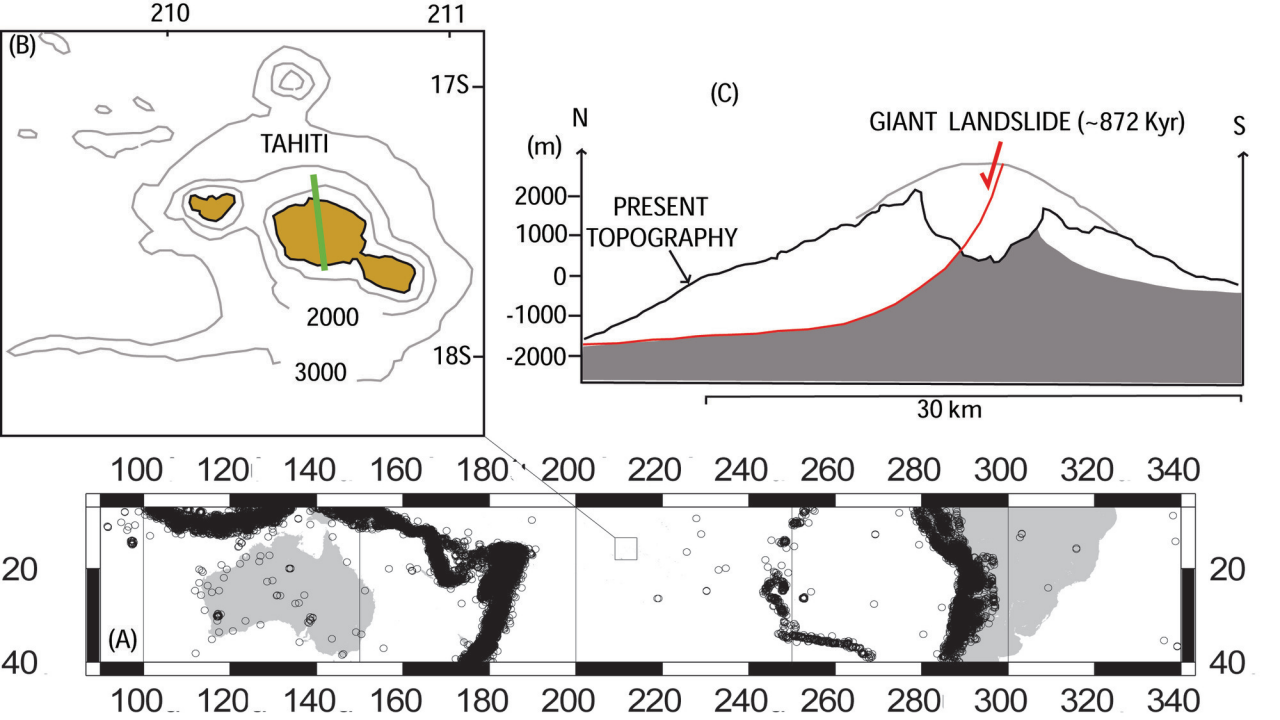
210
211
(B)
17S
TAHITI
2000
3000
18S
(C)
N
S
(m)
2000
1000
0
-1000
-2000
PRESENT
TOPOGRAPHY
GIANT LANDSLIDE (~872 Kyr)
30 km
100 120 140 160 180 200 220 240 260 280 300 320 340
20
40
(A)